ARTICLE

Hollow Silica Nanoparticles in UV–Visible Antireflection Coatings for Poly(methyl methacrylate) Substrates

Yi Du,[†] Lunet E. Luna,[†] Wui Siew Tan,[‡] Michael F. Rubner,[‡,*] and Robert E. Cohen[†,*]

[†]Department of Chemical Engineering, Massachusetts Institute of Technology and [‡]Department of Materials Science and Engineering and Center for Materials Science and Engineering, Massachusetts Institute of Technology

ABSTRACT We have demonstrated the utility of hollow silica nanoparticles in fabricating conformal thin film nanoporous antireflection (AR) coatings on both poly(methyl methacrylate) (PMMA) and glass substrates. Layer-by-layer (LbL) assembly was successfully used to produce ultrathin AR coatings on planar and textured surfaces. Hollow silica nanoparticles were synthesized to extend the range of apparent refractive indices possible in an AR coating, enabling the design of both single index and graded index AR coatings on PMMA substrates. The diameter and shell thickness of the silica nanoparticles are the two independent, controllable parameters that we manipulated to tune the refractive index of the coating. The AR coatings reduced the minimum reflection of PMMA from 7% to 0.5%, while the maximum transmission increased from 92% to 98% at the optimized wavelength region that could be adjusted from the near UV into the visible. Cross sectional SEM showed that conformal coatings can be achieved on grooved PMMA Fresnel lenses. AFM was used to study surface topography on flat substrates.

KEYWORDS: UV antireflection coating · hollow silica nanoparticles · layer-by-layer assembly · PMMA substrates

*Address correspondence to recohen@mit.edu, rubner@mit.edu.

Received for review May 11, 2010 and accepted June 3, 2010.

Published online June 10, 2010. 10.1021/nn101033y

Reflections from lenses in an optical system are undesirable because they contribute to a significant loss of transmitted light, which decreases the quality of the final image.[1−5] Any coating that is designed to reduce these reflections must also minimize extra scattering losses from the film, a requirement that is more difficult to achieve at lower wavelengths.[6−8] Hence, scattering of light within the coating can play an important role in AR films designed to operate in the near UV region, and it remains a challenge to maximize transmission in this region of the spectrum. To overcome this difficulty, a relatively smooth coating with small feature sizes (less than 1/10th of the target wavelength) is required. One example of the need for a UV AR coating can be found in telescopes used in space to study cosmic ray showers in the atmosphere.[9,10] Cosmic ray showers emit light in a very narrow band of the near UV region with wavelengths of 300−400 nm. In particular NASA intended to launch a telescope on the International Space Station to observe this phenomenon. The lens used in this telescope is a 2.5 m diameter PMMA Fresnel lens with micrometer-scale [~150 μm] grooves etched into its surface. Achieving a satisfactory AR coating on a PMMA Fresnel lens requires a process which employs low temperatures (PMMA $T_g \approx 105$ °C), can be scaled up to coat large substrates, and yields an AR film which is conformal, has a tunable and low refractive index, and exhibits very precise control of composition on the nanometer scale. In this paper, we will address the above requirements and demonstrate feasible coatings for this application.

UV AR coatings are found in nature, for example in transparent butterfly wings[11] and in the zero order grating surface of spiders.[12] These surfaces serve as protection against predators, namely birds and other species that have the ability to detect UV light. Transparent butterfly wings are composed of hollow nanostructures[11] which result in the high porosity necessary for UV AR properties (through very low refractive index) and the low scattering (the nanoscale pores are significantly smaller than the wavelength of UV light). Recognizing the success of these UV AR-based defense mechanisms in insects, we organized our experimental approach in an attempt to mimic their optical behavior.

Generally, AR properties are achieved through destructive interference between light reflected from the coating-substrate and the air-coating interfaces.[1,3,13−19] Minimum reflection from the coated surface is given by the Fresnel equation:

$$R_m = \left(\frac{n_c^2 - n_1 n_2}{n_c^2 + n_1 n_2}\right)^2 \quad (1)$$

where n_c, n_1, and n_2 are the refractive indices of the coating, medium, and substrate, respectively. For a given spectral range from wavelength λ_1 to λ_2, the design AR wavelength λ_0 is given by

$$\lambda_0 = \frac{2\lambda_1\lambda_2}{\lambda_1 + \lambda_2} \quad (2)$$

Minimum reflection can then be achieved by choosing an optical thickness ($n_c d_c$, where d_c is the coating thickness) which satisfies both the quarter wavelength design ($n_c d_c = \lambda_0/4$) and the Fresnel equation.[1,3,13−19] Precise control and tuning of both the refractive index and thickness of a coating layer are the two main challenges in developing an optimal UV AR coating. The most common way to obtain low refractive index materials is to use nanoporosity to reduce the apparent refractive index. For uniformly dense solid nanoparticles, the level of nanoporosity can be adjusted to some extent by changing the particle diameter and the packing arrangement. For example, by increasing the particle size from 7 to 63 nm, the apparent refractive index can be reduced from 1.35 to 1.18.[19,24−26] However, there is a practical limit on particle size since large enough particles will scatter light.[1,3−5,13,14,16−19,23−30] For example, Zhou *et al*. reported the creation of an omnidirectional AR thin film by using various spin coating techniques.[31−34] They successfully developed a good broadband AR coating for the visible region (>400 nm), but because of the large features they used, the scattering of light by the AR coating became unavoidable. Transmission efficiency was therefore largely compromised in near-UV wavelength regions.[28−34] Vacuum based plasma etching[35,36] has been reported to increase UV transmission for ultralow refractive index AR coatings.[33,37,38] However, the harsh plasma etching and the use of vacuum limits its utility for large plastic optics.

A versatile method is needed to homogeneously coat optics, for use in the UV region (200−400 nm wavelength region). In this paper, we discuss the use of hollow silica nanoparticles in an aqueous layer-by-layer (LbL) assembly process to create high performance UV AR coatings on PMMA lenses. The LbL technique is a well-known, versatile platform for preparing uniform thin films with a wide array of predesigned properties on the basis of sequential deposition of oppositely charged species.[15,20−23,39] It is a solution-based assembly process that ensures conformal coating of topographically complex surfaces and can also be scaled up to meet industrial needs *via* spray coating.[40] By controlled synthesis of hollow silica nanoparticles[41,42] and optimization of LbL assembly conditions,[15,20−23,39] we can tune the nanoparticle size and shell thickness as two independent variables in optical designs of the AR coatings in addition to the available choices from LbL assembly such as pH and number of bilayers deposited. The optical characteristics of conformally coated PMMA substrates with both single and graded index UV AR designs are described below.

RESULTS AND DISCUSSION

Synthesis of Hollow Silica Nanoparticles. There are a number of synthetic methods[41,42] that have been used to synthesize hollow silica nanoparticles. Wan and Yu reported a facile one-step solution-based synthetic route to produce high yields of hollow silica nanoparticles using controlled hydrolysis of TEOS *via* the Stöber method.[41] By implementing this method, we can control the nanoparticle's size and shell thickness independently, allowing us to design an AR coating which is optimized for a particular wavelength region. Changing the reactant ratios allows one to tune the diameter of the hollow silica nanoparticles from 50 to 400 nm and the wall thickness from 10 to 33 nm.[41−43] Using a similar synthesis protocol, we created hollow silica nanoparticles with quite uniform wall thicknesses. Figure 1 panels a, b, and c show hollow silica spheres synthesized with 0.27 g/2.25 mL, 0.36 g/1.5 mL, and 0.60 g/1.5 mL of PAA to TEOS (g to mL), respectively, while the amounts of ethanol, and ammonia as well as the synthesis conditions were held constant as described in the Experimental Section. The mean diameter and shell thickness were measured to be around 76 and 22 nm for sample **H80** (Figure 1a), 97 and 11 nm for sample **H150** (Figure 1b), and 228 and 22 nm for **H300** (Figure 1c). Table 1 shows the relationship between synthetic conditions and the resulting hollow silica nanoparticle structures. An attempt to produce thinner shells by further increasing the relative amount of PAA to TEOS to 0.36 g/0.9 mL resulted in ruptured particles as shown in Figure 1d. The minimum shell thickness achieved for stable hollow silica nanoparticles was 10 nm. From the data collected, we found that the amount of TEOS controls shell thickness, whereas the ratio of PAA to ethanol determines particle size. These findings are in agreement with the results of Wan and Yu.[41] To further understand the mechanism of the Stöber method, HRTEM was performed before rinsing the synthesized particles with DI water. We observed some ultrafine 5 nm silica nanoparticles within the cavity of the larger, hollow silica nanoparticles. These ultrafine silica nanoparticles and the silica shell itself densified and the silica shell shrank until there was no longer void space in the shell when exposed to the electron beam during TEM imaging. This observation may be due to the presence of both PAA and TEOS in the hollow silica structure before the DI water rinsing step, resulting in further TEOS precipitation to form very small nanoparticles. A detailed discussion and representative HRTEM images (Figure S1) are shown in the Supporting Information. Synthesized hollow silica nanoparticles, in particular samples **H80** and **H150** showed uniform shell thickness and a highly reproducible core−shell struc-

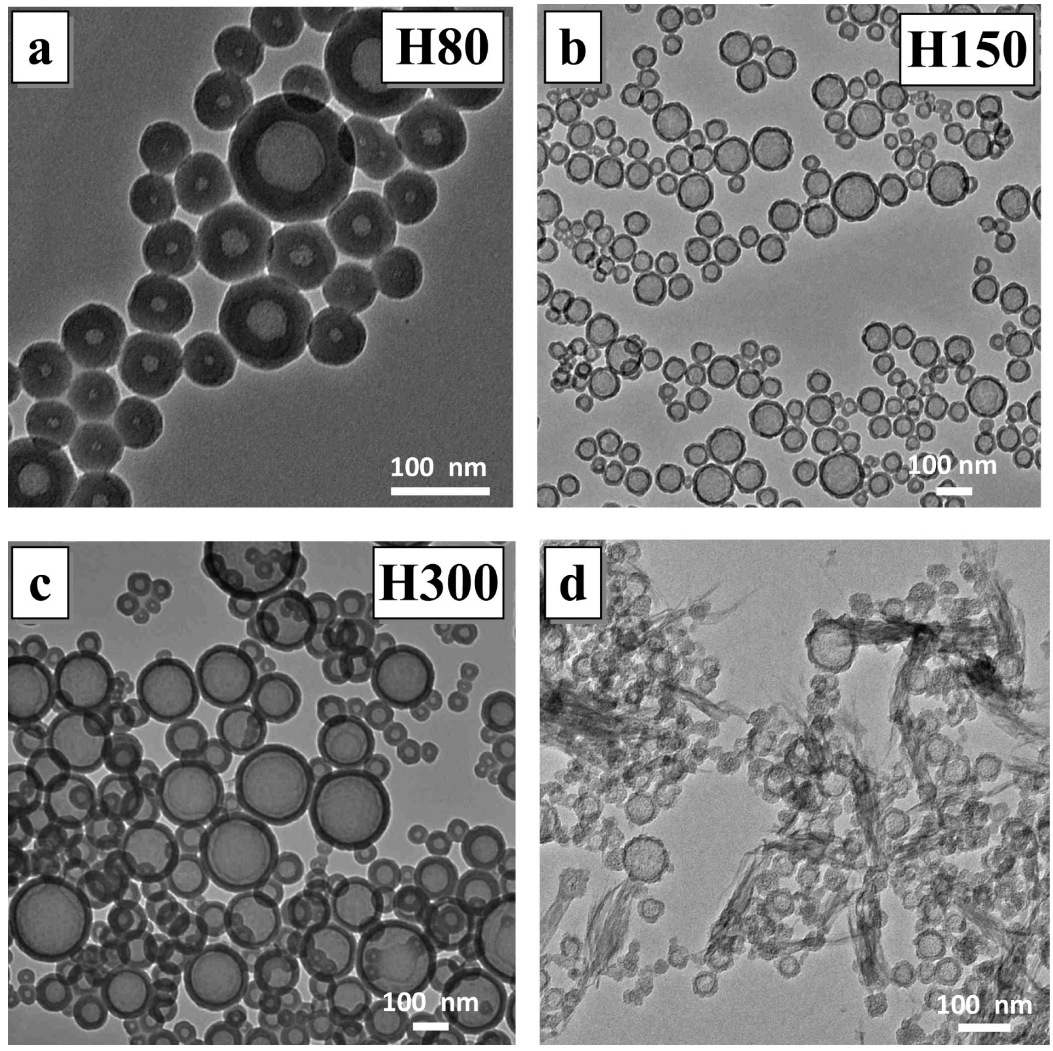

Figure 1. TEM images of the controlled synthesis of hollow silica with the varying amounts of PAA/TEOS: (a) 0.27 g/2.25 mL; (b) 0.36 g/1.50 mL; (c) 0.60 g/1.50 mL; and (d) 0.36 g/0.90 mL.

ture. Consequently, **H80** and **H150** were employed as starting materials for LbL assembly of a single index and graded index AR coatings, respectively.

Layer-by-Layer Assembly. Studies have shown that the pH of a nanoparticle suspension has a strong influence on its LbL deposition characteristics.[20−22,35,44,45] The suspension pH influences the average incremental bilayer thickness, refractive index, chemical composition, and film porosity,[20−22,35] all of which are key parameters which determine the AR performance. In this study, PAH and hollow silica nanoparticles (**H80** or **H150**) were assembled on glass or PMMA substrates to determine the average bilayer thickness and study the influence of pH on the assembled thin film. The pH of all the dipping solutions (PAH, rinsing water, and **H80** or **H150**) was adjusted to 3 or 6, and the film thickness was measured at 1, 3, 5, 7, and 9 bilayers. Ellipsometry results are plotted in Figure 2 to demonstrate the difference in coating thicknesses at pH 3 and 6. Together, Table 2 and Figure 2 summarize the influence of pH and substrate chemistry on LbL-assembled films.

In general, the multilayer film grows more rapidly at pH 3 than at pH 6 for both types of hollow silica nanoparticles (**H80** and **H150**) on both PMMA and glass substrates. Further disruption of film growth was observed when experiments were carried out at pH 9 (data not shown). Increasing the pH from 3 to 6 increases the

TABLE 1. Correlation of Synthetic Conditions for Hollow Silica Nanoparticles[a] to the Product Morphology. The Entries in the Table Correspond to Panels a, b, c, and d in Figure 1

	PAA (g)	TEOS (mL)	particle size (nm)[b]	shell thickness (nm)
a (**H80**)	0.27	2.25	76 ± 20	22 ± 2
b (**H150**)	0.36	1.50	97 ± 19	11 ± 3
c (**H300**)	0.60	1.50	76 ± 12 (60%)[c]	17 ± 3
			228 ± 101 (40%)[d]	22 ± 4
d	0.36	0.90	ruptured particles	ruptured particles

[a]Also added were 4.5 mL ammonium hydroxide solution, and 120 mL absolute ethanol (see Experimental Section for detail. [b]The particle size is an average from 50 nanoparticles in the TEM images from IMAGE J software. [c]Average size (probability) based on the small particles only. [d]Average size (probability) based on the large particles only.

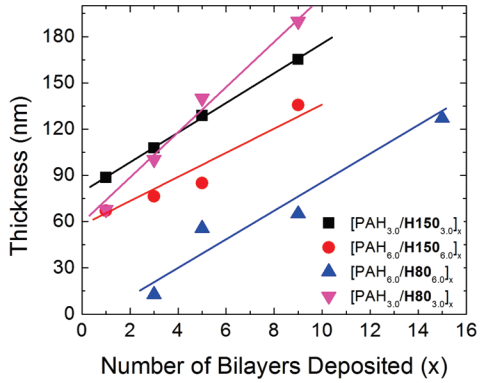

Figure 2. Growth curve studies by ellipsometry, where the thickness of the AR coating is plotted against the number of bilayers: (■) [PAH$_{3.0}$/H150**$_{3.0}$]; (●) [PAH$_{6.0}$/**H150**$_{6.0}$]; (▲) [PAH$_{6.0}$/**H80**$_{6.0}$]; (▼) [PAH$_{3.0}$/**H80**$_{3.0}$]. The slopes of the best-fit lines indicate the average bilayer thickness.**

charge density of silica nanoparticles (anionic species); hence fewer nanoparticles would be needed to achieve charge reversal on the previous layer, which decreases the incremental bilayer thickness. At an even lower pH (pH $<$ 3), the charge density is too low to effectively stabilize the silica nanoparticles, resulting in significant aggregation.[21,22] Comparing LbL growth at pH 3, 6, and 9, we found that the optimal conditions for deposition of these hollow silica nanoparticles occurs at pH 3, consistent with the findings of earlier work on LbL assembly of solid silica nanoparticles.[46,47]

Although most of the growth curves shown in Figure 2 do not pass through the origin, a linear trend is observed after the first (or third in the case of [PAH$_{6.0}$/**H80**$_{6.0}$]) bilayer deposition. Figure 2 shows how the bare PMMA substrate responds to coating with a single (or a few) bilayer(s) of hollow silica and PAH. For the [PAH$_{3.0}$/**H80**$_{3.0}$], [PAH$_{3.0}$/**H150**$_{3.0}$], and [PAH$_{6.0}$/**H150**$_{6.0}$] multilayers, a single bilayer deposition results in relatively complete coverage of the pristine PMMA surface with PAH and hollow silica nanoparticles, after which a fairly constant fractional coverage of the surface occurs at each deposition step.[20−22,35] The bilayer thickness increment shown in Table 2 is noticeably lower than the average size of the hollow silica nanoparticles (**H80**, ∼76 nm and **H150**, ∼97 nm). This observation indicates incomplete surface coverage at each deposition step. Also, the effect of pH on the bilayer thickness is more significant in the case of the smaller, thicker shelled **H80** nanoparticles than the larger **H150** nanoparticles with thinner shells.

Characterization of LbL Assemblies. In contrast to films made of solid nanoparticles, here overall film porosity consists of the intraparticle void space in addition to the spaces between particles. To determine the overall porosity of the coatings, [PAH$_{3.0}$/**H80**$_{3.0}$]$_{15}$ and [PAH$_{3.0}$/**H150**$_{3.0}$]$_{15}$ films were assembled on silicon substrates. The overall porosity of each film was determined by measuring the refractive index of the films in air and in water (n_{water} = 1.333, using *in situ* ellipsometry ($n_{f,1}$ = $pn_{f,air}$ + (1 − p)$n_{f,framework}$; where p is defined as the fractional porosity), and applying simple effective medium equations[35] to the measured values. The refractive index of the solid silica shell of the hollow particles was computed from the effective refractive index of the particles and the geometrical information obtained from SEM (Table 1). The calculated values of 1.49 and 1.45, for the amorphous silica walls of **H80** and **H150**, respectively, are in reasonable agreement with the range of reported silica refractive index values (1.45−1.54),[15,20−23,35] indicating that in the wet ellipsometry measurements water permeates into the hollow cores of the particles. Experiments were repeated using ethanol ($n_{ethoanol}$ = 1.361) as the liquid medium with essentially identical results. The overall LbL film porosities for [PAH$_{3.0}$/**H80**$_{3.0}$]$_{15}$ and [PAH$_{3.0}$/**H150**$_{3.0}$]$_{15}$ films were 64.5% and 75.1%, respectively. These values are much higher than those for previously reported porosities of LbL films based on solid nanoparticles which typically are around 50%.[15,20−23,35]

As demonstrated above, the additional void space within our hollow nanoparticles has opened a new window of parameter space for controlling the optical properties of LbL assembled thin films. Previous attempts to create low-index coatings using LbL assembly of nanoparticles have relied on the creation of void space between solid spheres during LbL deposition. A close packed layer of solid spheres has a porosity of about 26%, and to achieve a level of 76% porosity,

TABLE 2. Characteristics of the as-Synthesized Hollow Silica Nanoparticles (H80 or H150) on PMMA or Glass Substrates at pH 3 and pH 6

		PAH/H80		PAH/H150	
	pH	PMMA	glass	PMMA	glass
average incremental bilayer thickness (nm)[a]	3	16.0 ± 1.0	13.7 ± 1.2	9.6 ± 0.1	10.9 ± 0.7
	6	8.3 ± 1.4	4.7 ± 1.1	8.9 ± 1.5	13.9 ± 2.8
thickness at 9 bilayers[b]	3	192.7 ± 10.0	137.7 ± 13.5	165.5 ± 1.6	149.8 ± 6.7
	6	74.8 ± 21.0	94.4 ± 18.7	131.0 ± 15.6	133.3 ± 30.0
refractive index at 9 bilayers[a]	3	1.20 ± 0.01	1.19 ± 0.01	1.11 ± 0.05	1.10 ± 0.06
	6	1.17 ± 0.01	1.16 ± 0.01	1.10 ± 0.02	1.09 ± 0.04

[a]The standard deviation is calculated from spectroscopic ellipsometry. [b]All the data was linear fitted with a confidence ranged from 0.91 to 0.99; the thickness at 9 bilayers is then calculated by the fitted curved with a standard deviation calculated by propagation of uncertainty (if f(x) = A + Bx and the standard deviation of A and B are σ_A and σ_B respectively; the standard deviation of f(C): $\sigma_C^2 = \sigma_A^2 + C^{2*}\sigma_B^2$).

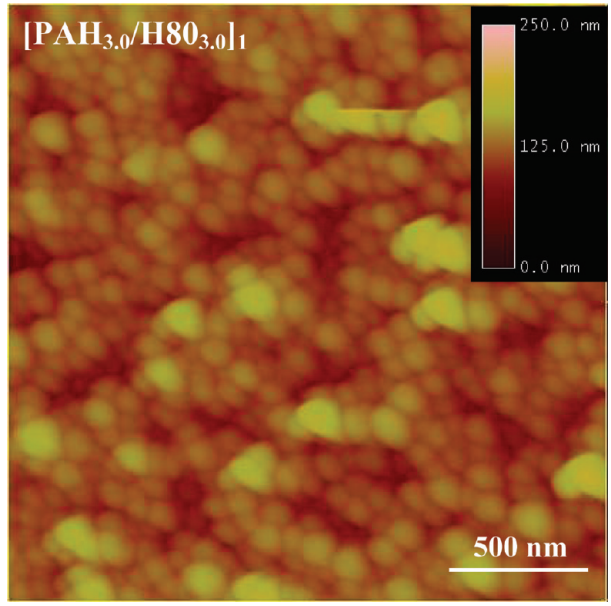

Figure 3. AFM image of $[PAH_{3.0}/\mathbf{H80}_{3.0}]_1$ on PMMA substrate.

roughly $^2/_3$ of the spheres would need to be removed. Such a loosely packed arrangement of solid spheres would be difficult to create by LbL self-assembly and even if made, would be mechanically fragile owing to the drastically reduced number of contact points between spheres. Using hollow particles circumvents the limitations presented by conventional means of controlling multilayer porosity (solely through changing the packing density of solid spherical particles), expanding our ability to achieve very high overall porosity and very low refractive index without reducing the number of sphere-to-sphere contacts to the point where the mechanical stability is compromised too much; a favorable circumstance recognized by Hoshikawa *et al*. in their recent work on hollow/mesoporous silica nanoparticle AR coatings in the visible range[6,47−49] In the work of Hoshikawa *et al*., a bar coating method is employed to apply either mesoporous or hollow silica nanoparticles directly onto glass substrates to achieve AR coatings. The highest porosity is 48% from this method and the optimum reflectance is lowered from 5% to 2% in the visible range.[6,47,49] By applying the LbL assembly method using designable hollow silica nanoparticles, our high porosity films produced using hollow silica nanoparticles reached up to 75% porosity, and were mechanically stable enough to withstand a simple paper/ethanol wipe test (see Supporting Information, Figure S2). Ongoing efforts are focused on improving the mechanical robustness further.

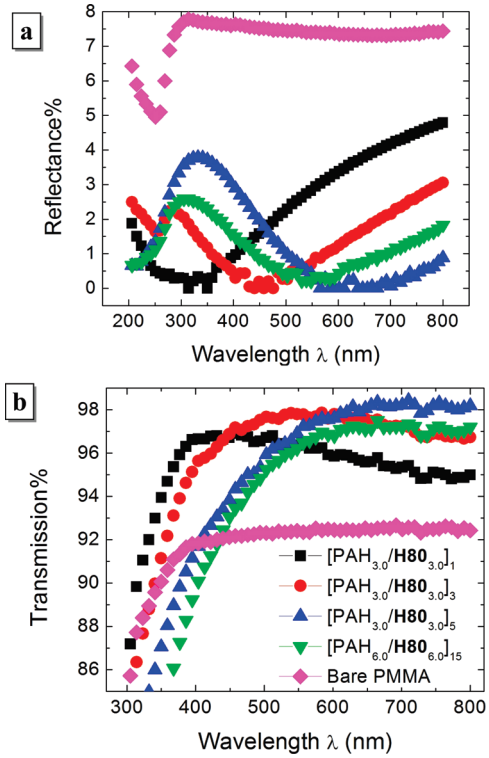

Figure 4. UV−vis reflection (a) and transmission (b) spectra for the single index design on PMMA substrates.

Antireflection Coating Optical Performance. For narrow bandwidth AR about a selected wavelength λ_0, excellent AR properties can be achieved with a single index coating of refractive index $n_c = (n_1 n_2)^{1/2}$ and thickness, $d_c = \lambda_0/4n_c$[3−5] where in this work $n_1 = 1.00$ is the refractive index of the medium (air) and $n_2 = 1.49$ is the value for PMMA. Thus a single layer AR coating's refractive index should be 1.22 with an optimal thickness of 74 nm when the target wavelength is 360 nm (near-UV). Given that there are no existing bulk materials that possess a refractive index of 1.22, we produced a nanoporous coating from the hollow silica nanoparticles **H80** (Table 1) using the layer-by-layer assembly technique described in the previous section. Nanoscale dimensions for both the constituent particles and the void spaces in the AR coating are required to minimize scattering from the coating in the near UV region of interest here. Hollow nanoparticles allowed us to develop the needed level of overall porosity without requiring an unusually sparse packing of the particles in the coatings. In general, we have found that increasing particle size polydispersity tends to increase the packing density and the refractive index of LbL nanoparticle films. Thus we believe that efforts to synthesize hollow nanoparticles with nearly monodisperse size distributions would further assist in the precise design and construction of novel optical coatings.

Figure 1a is a TEM image of the **H80** hollow silica nanoparticles with shell thickness 22 nm and mean diameter 76 nm, while Figure 3 is an AFM height image of a $[PAH_{3.0}/\mathbf{H80}_{3.0}]_1$ multilayer on a PMMA substrate. Analysis of the AFM data gives a rms roughness in the range of 17 nm, consistent with the requirement of sufficient smoothness to reduce scattering of light in the range of 300−400 nm. The measured optical performance of this single bilayer AR coating is shown in Figure 4a (reflection) and Figure 4b (transmission) in comparison with bare PMMA substrates and other PAH/

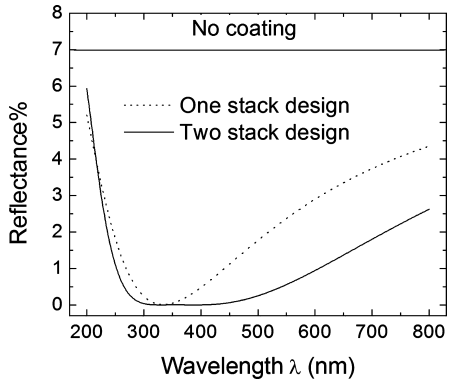

Figure 5. Simulated reflectance from AR coating on PMMA substrates using either graded (black) or single (red) refractive index design targeted for AR at wavelengths between 300 and 400 nm.

H80 constructs. The PMMA substrate control shows much poorer optical behavior, with about 7% reflection and 92% transmission over most of the near UV and visible region of the spectrum. By applying a single bilayer coating, excellent antireflection behavior in the near UV was obtained. The reflectance is essentially 0% at 340 nm, and scattering contributed by the coating is low as revealed by the transmission of 97% at 380 nm. By changing the number of bilayers deposited and the assembly pH, the AR coating can be optimized for different wavelengths (450, 500, and 600 nm) with 0% reflectance in each case. Figure S3 in the Supporting Information provides additional AFM images of some of the PAH/**H80** films that are represented in Figure 4. Figure S4 shows the optical behavior of these single stack AR coatings on glass substrates.

While a single refractive index coating is the simplest to create, its optimum AR efficacy is limited to incidence angles near 90° and persists over a relatively narrow region of wavelengths. A graded index coating generally offers superior AR performance. The simplest approximation to a continuously variable coating uses a two-stack design (Figure 6), with stacks further from the substrate having progressively lower refractive indices.

A two-stack AR coating requires high (n_H) and low (n_L) index regions with the same optical thickness equal to a quarter of the reference wavelength ($n_H d_H = \lambda_0/4$ and $n_L d_L = \lambda_0/4$).[3−5] The overall reflectance is then calculated by the characteristic matrix method,[3] where the refractive index for each stack is iterated in steps of 0.1 until a minimum integrated reflection over the 300−400 nm range is obtained. The calculated results in Figure 5 show the enhanced performance of the two-stack design on PMMA compared to that of the best single index coating. The optimal two-stack design includes a 67 nm bottom layer (the layer in contact with substrate) with a refractive index of 1.35, while the top layer (the layer in contact with air) must be 81 nm thick and have a very low index of 1.11. Figure 6 provides schematic sketches of the two AR designs.

Our modeling results show that the optical performance of the two-stack design is sensitive to deviations from the target values of refractive index in the two regions, but relatively insensitive to nonoptimal thicknesses. Figure S5 provides some examples of these modeling sensitivity studies including the influence of varying film thicknesses and refractive indices of the two stack design.

To produce the higher refractive index stack of the two-stack design, smaller nanoparticles with higher refractive indices (SM-30: anionic, 7 nm SiO_2, $n \approx 1.5$. ZrO_2: cationic, 7 nm ZrO_2, $n \approx 2.1$) were employed.[20−22] By adjusting the pH and the number of bilayers deposited, an all-nanoparticle stack with a high refractive index (RI = 1.35; thickness = 67 nm) was successfully achieved using nine bilayers of [$ZrO_{2\ 3.0}$/SM-$30_{3.0}$]. For the very low index top layer we employed the **H150** hollow silica nanoparticles described in Table 1 and shown in the TEM image Figure 1c. The large average diameter (97 nm) and low wall thickness (11 nm) of these hollow nanoparticles facilitated the production of the required ultralow index stack *via* LbL assembly. Specifically we found that the six-bilayer top stack [$PAH_{3.0}$/**H150**$_{3.0}$]$_6$ gave optimal AR performance for the two-stack design on PMMA substrates. It is worth mentioning that the thickness of the top stack was much thinner than expected from growth studies on the [$PAH_{3.0}$/**H150**$_{3.0}$]
system on silicon. This is likely due to substrate influence because the second stack is built on top of a [$ZrO_{2\ 3.0}$/SM-$30_{3.0}$]$_9$ stack. Figure 7a shows a cross-sectional SEM image of this two-stack coating on PMMA and Figure 7b shows an AFM height image of the top surface. The average thickness for layer in contact with

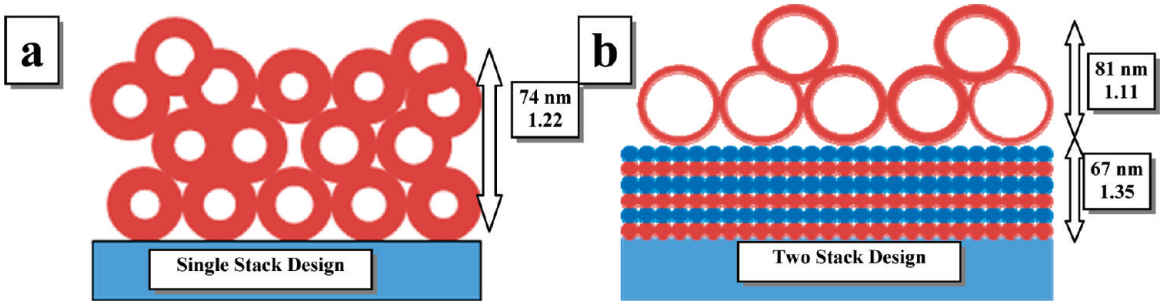

Figure 6. Schematic showing how layers are stacked in the one- and two-stack AR design.

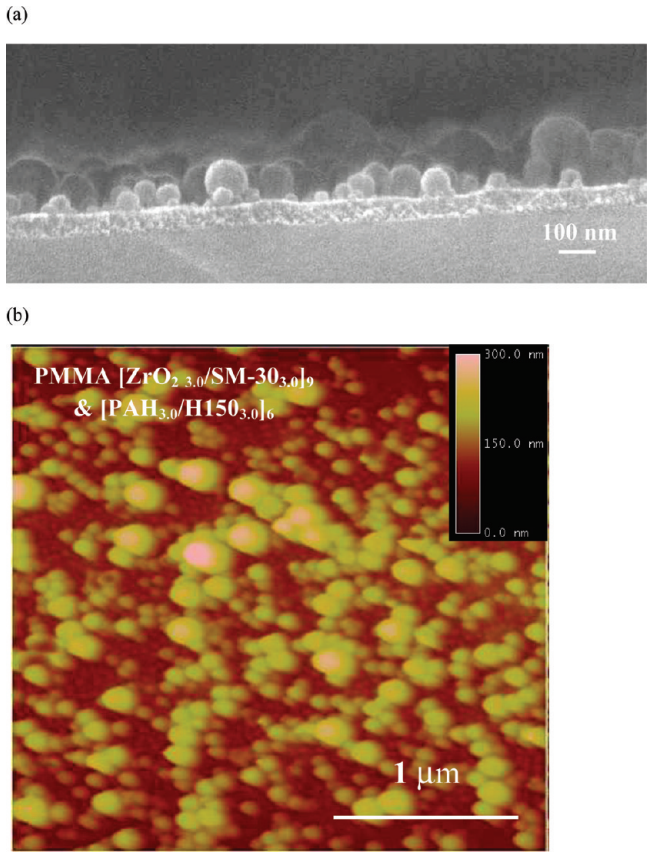

Figure 7. Graded index AR design consisting of $[ZrO_{2\ 3.0}/SM\text{-}30_{3.0}]_9$ followed by $[PAH_{3.0}/\mathbf{H150}_{3.0}]_6$ on a PMMA substrate: (a) SEM cross sectional image and (b) AFM image of the plan view topography.

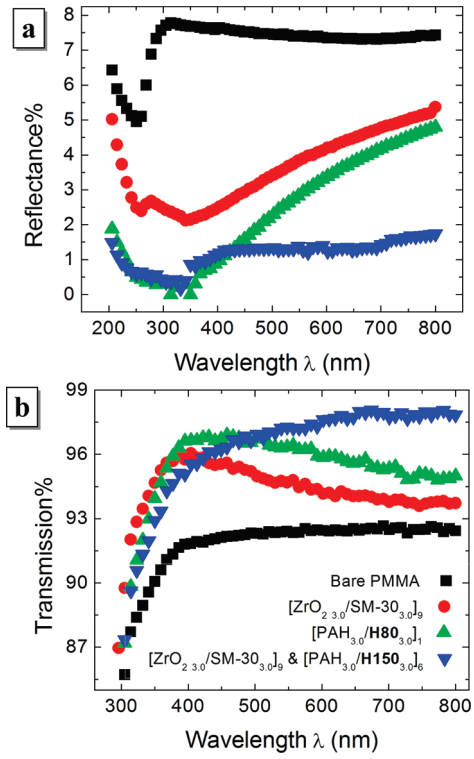

Figure 8. Selected UV−vis (a) reflection spectra and (b) transmission spectra for one- and two-stack design on PMMA, assembled at pH 3.

substrate and layer in contact with air is 70 and 90 nm, respectively, from Figure 7a, which is consistent with the calculation. As shown in Figure 8, reflection was reduced to nearly 0% at 320 and 450 nm on PMMA and glass substrates, respectively. A very wide AR regime is observed with less than 2% reflectance between 200 and 800 nm as compared to the single stack design as reference. However the transmission is compromised at short wavelengths.

Compared to the 76 nm diameter particles used in the single stack coating, the larger 97 nm diameter hollow silica nanoparticles produce significant low wavelength scattering, most likely arising from the comparatively large roughness (40 nm rms roughness for the two stack coatings vs 17 nm rms roughness for the single-stack design) as well as from Mie and Rayleigh scattering from the particles themselves.

All of the work reported above was executed on flat substrates. To test the versatility of our novel AR coatings and the utility of LbL processing, the performance of a single-stack design on the grooved surface of PMMA Fresnel lenses was examined (see Supporting Information).[40] We have found that the grooved surfaces of PMMA Fresnel lenses can be conformally coated and make LbL feasible even on nonplanar substrates.

CONCLUSIONS

We have successfully synthesized hollow silica nanoparticles with variable particle size and shell thickness to achieve UV AR coatings *via* single and graded index designs. When we deposited these nanoparticles onto substrates, specifically glass and PMMA, their internal voids allowed the assembly of coatings with porosities as high as 75% and an apparent refractive indices as low as 1.11. Single index AR coatings can be achieved with optimized AR performance at any wavelength between 300 and 650 nm; reflection near the targeted wavelength was reduced from 7% to 0% and transmission was increased from 92% to 97%. In addition, a graded index AR design was also successfully achieved, yielding reflectance of below 2% over the whole UV−vis region (200−800 nm).

EXPERIMENTAL SECTION

Materials. Silica nanoparticles Ludox SM-30 (30 wt % SiO_2 suspension in water, average particle size 7 nm) were purchased from Sigma-Aldrich (St. Louis, MO). Tetraethoxysilane (TEOS, 98% reagent grade), poly(acrylic acid) (PAA, $M_w \approx 5000$; 50 wt % in aqueous solution) was purchased from Polysciences, Inc. Poly(allylamine hydrochloride) (PAH, $M_w \approx 56\,000$) and ammonium hydroxide (28% NH_3 in water) were purchased from Sigma-Aldrich. Zirco-

nium(IV) oxide (20 wt % ZrO_2 suspension in water, average particle size = 7 nm) was purchased from Alfa Aesar. The information on average size of the nanoparticles was provided by the suppliers. Glass slides were purchased from VWR International, and UV transparent PMMA substrates were provided by Agiltron, Inc.

Synthesis of Hollow Silica Nanoparticles. Uniform hollow silica spheres were prepared by a modified Stöber method.[41,42] First, 0.27 g of PAA dissolved in 4.5 mL of ammonium hydroxide was mixed with 90 mL of absolute ethanol, followed by injection of 5 TEOS aliquots totaling 2.25 mL at 1 h time intervals under vigorous magnetic stirring at room temperature.[41,42] After 10 h, a white colloid containing 80 nm hollow silica nanoparticles formed. This colloid was centrifuged several times with deionized water (>18 MΩ · cm, Millipore Milli-Q) and then dried at room temperature. Hollow silica spheres with different diameters and/or wall thicknesses were prepared by varying the concentrations of polyelectrolyte in ammonia and/or TEOS in ethanol (Table 1). During synthesis, vigorous continuous stirring is crucial for the formation of hollow silica nanoparticles.

Assembly of PAH/Hollow SiO_2 Nanoparticle Multilayers. Sequential adsorption of PAH and hollow SiO_2 nanoparticles onto glass slides, silicon wafers, or PMMA substrates was performed using an automated dipping machine.[16,20−22] The concentration of each nanoparticle suspension was 0.03 wt % and the concentration of PAH was 10 mM (based on the repeat unit). The pH of each nanoparticle suspension was adjusted using 1.0 M HCl or NaOH. Glass substrates were sonicated in 1.0 M NaOH for 15 min and in DI water for 1 h. PMMA substrates were sonicated in 2 vol% detergent solution for at least 1 h and then in DI water for an additional hour. Deionized water was used for all solutions and rinse baths and was adjusted to the same pH as the dipping solution. The dipping time in each nanoparticle solution was 10 min followed by three rinse steps (2, 1, and 1 min) in deionized water.

Characterization. Transmission and reflection measurements were performed between 200 and 800 nm using a Varian Cary 500i spectrophotometer. Spectroscopic ellipsometry (M2000-D, J. A.Woollam Co.) was used to determine the thickness and refractive index of the coatings. These values of thickness and refractive index are influenced by the roughness of the films and possibly in some cases by gradients in packing density. Therefore they should be viewed as internally consistent values of effective thickness and index that were used to guide the AR coating design calculations. Results were collected from 300 to 900 nm at a 70° angle of incidence. The morphology of a coating surface was investigated with AFM by using a Nanoscope IV, Dimension 3000 AFM microscope (Digital Instruments, Santa Barbara) in tapping mode in air. Transmission electron microscopy (TEM) was performed using a JEOL 200CX operating at 200 kV. Scanning electron microscopy (SEM) was performed using a JEOL 6320FV field emission high-resolution SEM at an acceleration voltage of 10 kV. The samples were coated with 15 nm of Au/Pd prior to SEM imaging.

Acknowledgment. This work was supported by Agiltron, Inc. through NASA SBIR Grant Number NNM08AA03C. We thank the Center for Materials Science and Engineering (CMSE) and the Institute for Soldier Nanotechnologies (ISN) for use of their characterization facilities. We also thank Dr. Yong Zhang of CMSE for his assistance with the SEM measurements, Zekeriyya Gemici for his help with the optical modeling, and Sangyup Song, Qingwu Wang in Agiltron, Inc. for useful discussions.

Supporting Information Available: Detail discussion about hollow silica nanoparticle synthesis and its formation mechanism and the application of LbL assembly method onto nonplanar PMMA substrates were included in the Supporting Information. This materials is available free of charge *via* the Internet at http://pubs.acs.org.

REFERENCES AND NOTES

1. Yanagishita, T.; Nishio, K.; Masuda, H. Anti-Reflection Structures on Lenses by Nanoimprinting Using Ordered Anodic Porous Alumina. *Appl. Phys. Express* **2009**, *2*, 022001−3.
2. Xi, J.; Schubert, M. F.; Kim, J. K.; Schubert, E. F.; Chen, M.; Lin, S.; Liu, W; Smart, J. A. Optical Thin-Film Materials with Low Refractive Index for Broadband Elimination of Fresnel Reflection. *Nat. Photon.* **2007**, *1*, 176–179.
3. Schallenberg, U. B. Antireflection Design Concepts with Equivalent Layers. *Appl. Opt.* **2006**, *45*, 1507–1514.
4. Laux, S.; Mann, K.; Granitza, B.; Kaiser, U.; Richter, W. Antireflection Coatings for UV Radiation Obtained by Molecular-Beam Deposition. *Appl. Opt.* **1996**, *35*, 6216–6218.
5. Yoldas, B. E.; O'Keeffe, T. W. Antireflective Coatings Applied from Metal-Organic Derived Liquid Precursors. *Appl. Opt.* **1979**, *18*, 3133–3138.
6. Joo, W.; Kim, H. J.; Kim, J. K. Broadband Antireflection Coating Covering from Visible to Near Infrared Wavelengths by Using Multilayered Nanoporous Block Copolymer Film. *Langmuir* **2009**, *26*, 5110–5114.
7. Hoshikawa, Y.; Yabe, H.; Nomura, A.; Yamaki, T.; Shimojima, A.; Okubo, T. Mesoporous Silica Nanoparticles with Remarkable Stability and Dispersibility for Antireflective Coatings. *Chem. Mater.* **2010**, *22*, 12–14.
8. Wang, Y.; Chen, N.; Zhang, X.; Yang, X.; Bai, Y.; Cui, M.; Wang, Y.; Chen, X.; Huang, T. Ag Surface Plasmon Enhanced Double-Layer Antireflection Coatings for GaAs Solar Cells. *J. Semicond.* **2009**, *30*, 072005−5.
9. Greisen, K. Cosmic Ray Showers. *Ann. Rev. Nucl. Part. Sci.* **1960**, *10*, 63–108.
10. Abu-Zayyad, T.; Al-Seady, M.; Belov, K.; Bird, D. J.; Boyer, J.; Chen, G.; Clay, R. W.; Dai, H. Y.; Dawson, B. R.; Ho, Y.; *et al.* The Prototype High-Resolution Fly's Eye Cosmic Ray Detector. *Nucl. Instrum. Methods Phys. Res., Sect. A* **2000**, *450*, 253–269.
11. Yoshida, A.; Kosaku, A.; Miyamoto, K. Antireflective Nanoprotuberance Array in the Transparent Wing of a Hawkmoth, Cephonodes Hylas. *Zoo. Soc.* **1997**, *14*, 737–741.
12. Parker, A. R.; Hegedus, Z. Diffractive Optics in Spiders. *J. Opt. A: Pure Appl. Opt.* **2003**, *5*, S111–S116.
13. Zhang, F.; Yang, W.; Pang, A.; Wu, Z.; Qi, H.; Yao, J.; Fan, Z. Shao, Annealing Effects On the Optical and Structural Properties of Al_2O_3/SiO_2 Films as UV Antireflection Coatings on 4H-SiC Substrates. *J. Appl. Surface Sci.* **2008**, *254*, 6410–6415.
14. Yamaguchi, N.; Tadanaga, K.; Matsuda, A.; Minami, T.; Tatsumisago, M. Antireflective Properties of Flowerlike Alumina Thin Films on Soda-Lime Silica Glass Substrates Prepared by the Sol−Gel Method with Hot Water Treatment. *Thin Solid Films* **2007**, *515*, 3914–3917.
15. Podsiadlo, P.; Sui, L.; Elkasabi, Y.; Burgardt, P.; Lee, J.; Miryala, A.; Kusumaatmaja, W.; Carman, M. R.; Shtein, M.; Kieffer, J.; Lahann, J.; Kotov, N. A. Layer-by-Layer Assembled Films of Cellulose Nanowires with Antireflective Properties. *Langmuir* **2007**, *23*, 7901–7906.
16. Wu, Z; Walish, J.; Nolte, A.; Zhai, L.; Cohen, R. E.; Rubner, M. F. Deformable Antireflection Coatings from Polymer and Nanoparticle Multilayers. *Adv. Mater.* **2006**, *18*, 2699–2702.
17. Park, M. S.; Lee, Y.; Kim, J. K. One-Step Preparation of Antireflection Film by Spin-Coating of Polymer/Solvent/Nonsolvent Ternary System. *Chem. Mater.* **2005**, *17*, 3944–3950.
18. Asghar, M. M.; Khan, M. B.; Naseem, S.; Khan, Z. A. Design and Preparation of Antireflection Films on Glass Substrate. *Turk. J. Phys.* **2005**, *29*, 43–53.
19. Hattori, H. Antireflection Surface with Particle Coating Deposited by Electrostatic Attraction. *Adv. Mater.* **2001**, *13*, 51–54.
20. Gemici, Z.; Schwachulla, P. I.; Williamson, E. H.; Rubner, M. F.; Cohen, R. E. Targeted Functionalization of Nanoparticle Thin Films *via* Capillary Condensation. *Nano Lett.* **2009**, *9*, 1064–1070.
21. Lee, D.; Omolade, D.; Cohen, R. E.; Rubner, M. F. pH-Dependent Structure and Properties of TiO_2/SiO_2 Nanoparticle Multilayer Thin Films. *Chem. Mater.* **2007**, *19*, 1427–1433.

22. Lee, D.; Gemizi, Z.; Rubner, M. F.; Cohen, R. E. Multilayers of Oppositely Charged SiO_2 Nanoparticles: Effect of Surface Charge on Multilayer Assembly. *Langmuir* **2007**, *23*, 8833–8837.
23. Zhang, L.; Li, Y.; Sun, J.; Shen, J. Mechanically Stable Antireflection and Antifogging Coatings Fabricated by the Layer-by-Layer Deposition Process and Postcalcination. *Langmuir* **2008**, *24*, 10851–10857.
24. Schubert, M. F.; Mont, F. W.; Chhajed, S.; Poxson, D. J.; Kim, J. K.; Schubert, E. F. Design of Multilayer Antireflection Coatings Made from Co-sputtered and Low-Refractive-Index Materials by Genetic Algorithm. *Opt. Express* **2008**, *16*, 5290–5298.
25. Zhao, Q.; Dong, Y.; Wang, P.; Zhao, X. CeO_2-TiO_2/SiO_2 Antireflecting and UV-Shielding Double-Functional Films Coated on Glass Substrates Using Sol−Gel Method. *J. Rare Earths* **2007**, *25*, 64–67.
26. Tikhonravov, A. V.; Trubetskov, M. K.; Amotchkina, T. V.; Kokarev, M. A.; Kaiser, N.; Stenzel, O.; Wilbrandt, S.; Gäbler, D. New Optimization Algorithm for the Synthesis of Rugate Optical Coatings. *Appl. Opt.* **2006**, *45*, 1515–1524.
27. Ulrike, S.; Norbert, K.; Uwe, B. S. AR-hard Broadband Antireflective Coatings Generated by a Controlled Needle-Optimization Technique. *Opt. Soc. Am.* **2004**, p TuB2.
28. Schulz, U.; Schallenberg, U. B.; Kaiser, N. Antireflection Coating Design for Plastic Optics. *Appl. Opt.* **2002**, *41*, 3107–3110.
29. Dobrowolski, J. A.; Tikhonravov, A. V.; Trubetskov, M. K.; Sullivan, B. T.; Verly, P. G. Optimal Single-Band Normal-Incidence Antireflection Coatings. *Appl. Opt.* **1996**, *35*, 644–658.
30. Barnes, G. A.; Flaim, T. D.; Jones, S. F.; Bruce, J.; Dudley, W.; Koester, D. A.; Peters, C. R. Bobbio, Antireflective Coating for Deep UV Lithography Process Enhancement. *Polym. Eng. Sci.* **1992**, *32*, 1578–1582.
31. Zhou, W.; Tao, M.; Chen, L.; Yang, H. Microstructured Surface Design for Omnidirectional Antireflection Coatings on Solar Cells. *J. Appl. Phys.* **2007**, *102*, 103105-1–103105-9.
32. Wang, Y.; Tummala, R.; Chen, L.; Guo, L. Q.; Zhou, W.; Tao, M. Solution-Processed Omnidirectional Antireflection Coatings on Amorphous Silicon Solar Cells. *J. Appl. Phys.* **2009**, *105*, 103501-1–103501-6.
33. Chen, L.;Yang, H.; Tao, M.; Zhou, W. *Optical Modeling and Measurements for Solar Energy Systems II*, 1st ed.; SPIE: San Diego, CA, 2008; Vol. 7046, p 704608.
34. Tao, M.; Zhou, W.; Yang, H.; Chen, L. Surface Texturing by Solution Deposition for Omnidirectional Antireflection. *Appl. Phys. Let.* **2007**, *91*, 081118-1−081118-3.
35. Huang, Y.; Chattopadhyay, S.; Jen, Y.; Peng, C.; Liu, T.; Hsu, Y.; Pan, C.; Lo, H.; Hsu, C.; Chang, Y.; Lee, C.; Chen, K.; Chen, L. Improved Broadband and Quasi-omnidirectional Antireflection Properties with Biomimetic Silicon Nanostructures. *Nat. Nano* **2007**, *2*, 770–774.
36. Chen, Q.; Hubbard, G.; Shields, P. A.; Liu, C.; Allsopp, D. W. E.; Wang, W. N.; Abbott, S. Broadband Moth-Eye Antireflection Coatings Fabricated by Low-Cost Nanoimprinting. *Appl. Phys. Lett.* **2009**, *94*, 263118-1–263118-13.
37. Li, Y.; Zhang, J.; Zhu, S.; Dong, H.; Jia, F.; Wang, Z.; Sun, Z.; Zhang, L.; Li, Y.; Li, H.; Xu, W.; Yang, B. Biomimetic Surfaces for High-Performance Optics. *Adv. Mater.* **2009**, *21*, 4731–4734.
38. Schubert, E. F.; Kim, J. K.; Xi, J. Low-Refractive-Index Materials: A New Class of Optical Thin-film Materials. *Phys. Stat. Sol. (b)* **2007**, *244*, 3002–3008.
39. Lee, D.; Rubner, M. F.; Cohen, R. E. All-Nanoparticle Thin-Film Coatings. *Nano Lett.* **2006**, *6*, 2305–2312.
40. Agiltron. SPALAS (Spray Assisted Layer-by-layer Assembly) Coating System. July 2009. http://www.agiltron.com/PDFs/SPALASTM.pdf
41. Wan, Y.; Yu, S. Polyelectrolyte Controlled Large-Scale Synthesis of Hollow Silica Spheres with Tunable Sizes and Wall Thicknesses. *J. Phys. Chem. C* **2008**, *112*, 3641–3647.
42. Chen, M.; Wu, L.; Zhou, S.; You, B. A Method for the Fabrication of Monodisperse Hollow Silica Spheres. *Adv. Mater.* **2006**, *18*, 801–806.
43. Tissot, I.; Reymond, J. P.; Lefebvre, F.; Bourgeat-Lami, E. SiOH-Functionalized Polystyrene Latexes. A Step toward the Synthesis of Hollow Silica Nanoparticles. *Chem. Mater.* **2002**, *14*, 1325–1331.
44. Cao, F.; Li, D. Morphology-Controlled Synthesis of SiO_2 Hollow Microspheres Using Pollen Grain as a Biotemplate. *Biomed. Mater.* **2009**, *4*, 025009−6.
45. Zhang, L.; Li, Y.; Sun, J.; Shen, J. Layer-by-Layer Fabrication of Broad-Band Superhydrophobic Antireflection Coatings in Near-Infrared Region. *J. Colloid Interface Sci.* **2008**, *319*, 302–308.
46. Iler, R. Multilayers of Colloidal Particles. *J. Colloid Interface Sci.* **1966**, *21*, 569–594.
47. Lvov, Y.; Ariga, K.; Ichinose, I.; Kunitake, T. Alternate Assembly of Ordered Multilayers of SiO_2 and Other Nanoparticles and Polyanions. *Langmuir* **1997**, *13*, 6195–6203.
48. Ohata, K.; Yoshihara, T. Japan Patent P2002-265866A, 2002.
49. Chen, Y.; Kang, E; Neoh, K. G.; Greiner, A. Preparation of Hollow Silica Nanospheres by Surface-Initiated Atom Transfer Radical Polymerization on Polymer Latex Templates. *Adv. Funct. Mater.* **2005**, *15*, 113–117.